Thermal Pressure in the Laser Heated Diamond Anvil Cell: A Quantitative Study and Implications for the Density vs. Mineralogy Correlation of the Mantle

Connor Ethan Yen[1),2)] Quentin Williams[3)] and Martin Kunz[1)]

[1] Advanced Light Source, Lawrence Berkeley National Lab, Berkeley CA 94720.

[2] Mathematics, University of California, Berkeley, CA 94720.

[3] Earth and Planetary Sciences, University of California, Santa Cruz, CA 95064.

Corresponding author: Martin Kunz (mkunz@lbl.gov)

Key Points:

- Thermal pressure and its gradient in a diamond anvil cell has been measured and found close to the magnitude expected based on the thermodynamic limit.
- The observed gradients in thermal pressure are very steep. This can lead to an underestimation of the real pressure experienced by a heated sample.
- Underestimating the thermal pressure by only 20 % can have a significant effect on inferred deep mantle iron contents derived from laser heated diamond anvil cell experiments.

Abstract

Thermal pressure is an inevitable thermodynamic consequence of heating a sample that is volume constrained within the diamond anvil cell. Its possible influences on experimentally determined density-mineralogy correlations are well known, yet the effect itself has never been experimentally measured. We present here the first quantitative measurements of the magnitude and gradient of thermal pressure in a laser heated diamond anvil cell (LHDAC). The observed thermal pressure is strongly localized and follows the distribution of the laser hotspot. The magnitude of the thermal pressure is of the order of the thermodynamic thermal pressure ($\alpha K_T \mathrm{d}T$) with gradients between 0.5 – 1.0 GPa/10 μm. Remarkably, we measure a steep gradient in thermal pressure even in a sample that is heated close to its melting line. This imposes consequences for pressure determinations during pressure-volume-temperature (PVT) equation of state measurements when using a LHDAC. We show that an incomplete accounting of thermal pressure in PVT experiments can lead to biases in the coveted depth versus mineralogy correlation. However, the ability to spatially resolve thermal pressure in a LHDAC opens avenues to measure difficult-to-constrain thermodynamic derivative properties, which are important for comprehensive thermodynamic descriptions of the interior of planets.

Plain Language Summary

The primary window into the interior of the Earth below ~10 km depth are earthquake waves that give us a 3-dimensional elasticity/density image of the planet. In order to translate this into a geological model of the Earth, we need to know the physical and chemical response of rocks with the composition of the Earth's interior at high pressures and temperatures. This is achieved by experiments in which samples are subjected to the high pressure and temperatures of the deep Earth using laser heated diamond anvil cells. A long standing problem of such experiments is a hard to quantify pressure term caused by the heating of the sample. This paper for the first time experimentally quantifies the thermal pressure distribution in a typical experiment and explores the effect of its incomplete knowledge on the deduced mineralogical composition of the Earth.

1 Introduction

Over the past ~ 25 years, laser heated diamond anvil cells have played an important role in experimentally accessing the conditions of the interior of the Earth and Earth-sized planets (e.g. Williams et al. [1991]; Fiquet et al. [1998];Mao et al. [2004]; Ismailova et al. [2016]; Bassett [2016]). The technique allows experimental simulation of pressures and temperatures relevant to the interior of the Earth, while allowing in-situ probing of structural and thermo-elastic properties of samples using a large portion of the electromagnetic spectrum (e.g. Shen and Mao [2016]; Mezouar et al. [2017]). Despite the maturity of this technique, there persist remarkable discrepancies between results reported from different experiments (e.g. Komabayashi and Fei [2010]), and also between experiments and theory (e.g. Dorogokupets et al. [2015]).

From an experimental perspective, the sources of discrepancies in a LHDAC experiment are often associated with difficulties in measuring the pressure and temperature of the sample chamber. A second source of experimental uncertainty stems from the difficulty in positioning the probe (e.g. an X-ray beam) at a position of well-defined pressure and temperature within a sample volume with high thermal gradients (~10^4 K/mm) (e.g. Panero and Jeanloz [2001];

Kavner and Nugent [2008]) and non-hydrostatic stress conditions (e.g. Meng et al. [1993]). Differences in sample preparation cause additional elements of limited reproducibility (e.g. Marquardt and Marquardt [2012]), as does unrecognized contamination (e.g. Morard et al. [2017]). Here, we probe an additional long-recognized but largely experimentally uncharacterized measurement uncertainty in such P-V-T experiments. On localized heating, the thermal expansion of the sample generates an increase in pressure that can vary between zero (for an isobaric case, in which the sample container expands in accord with the thermal expansion) and $\alpha K_T \Delta T$ for the isochoric case, where α is the thermal expansion, K_T the isothermal bulk modulus, and ΔT the change in temperature. For the isobaric case, the manifestation of the sample expansion could be constrained by the pressure decrease in the post-heated sample; the isochoric case, or cases that are intermediate between isobaric and isochoric, are far more difficult to accurately characterize. This pressure change is far from trivial: for large temperature changes imposed on the relatively stiff oxides that comprise Earth's mantle, the magnitude of this isochoric pressure perturbation can be of the order of 10 GPa.

This pressure perturbation associated with localized heating is commonly referred to as thermal pressure (P_{th}). The thermal pressure is unrecorded in experimental set-ups where pressure is determined before and/or after the laser-heating event by using, for example, ruby fluorescence spectrometry. There is the potential ability to determine an average thermal pressure in experiments in which an internal calibrant (such as Pt) is embedded within the laser-heated spot and is monitored at high temperatures, but such single-location determinations could average across undetermined gradients in the thermal pressure. Indeed, the combination of the laser heated material's finite shear strength and the temperature gradient produced by the focused laser spot produces a spatial gradient in thermal pressure which is generally thought to be roughly of the same order as the size of the laser-heated spot: this supposition has therefore influenced the size of the probes that have been deployed to determine the P-V-T relations of Earth materials.

The possible role of thermal pressure in laser-heated diamond cell experiments has long generated estimates of its possible peak magnitude based on thermodynamics or observed pressure relaxation (e.g., Andrault and Fiquet [2001]). However, until now, no experiments have been conducted that measured the spatial variation in thermal pressure *in situ* across a laser-heated sample. In short, the spatial variation of thermal pressure quantifies both perturbations to the P-V-T state of a laser-heated sample, and the probe diameters needed to minimize pressure gradients across high-pressure, laser-heated samples.

The treatment of thermal pressure has been examined largely from a theoretical perspective. Heinz [1990] was the first to quantitatively address this issue from such a theoretical point of view. He estimated a P_{th} of ~ 2 - 10 GPa for a spherical Gaussian hot spot with T_{max} = 2000 K, a thermal expansivity $\alpha = 4 \times 10^{-5}$/K, Poisson's ratio $\nu = 0.25$, and Young's modulus E = 200 GPa. These calculations were done for various ratios of hot-spot to sample size for two scenarios: the case of a free surface boundary condition (which implies constant pressure at the surface), and the case of a constant volume. Calculated values for P_{th} (~ 4 to 5 GPa) for small hot spot sizes were very similar in both scenarios, indicating a local nature of P_{th} with high pressure gradients associated with the laser-heated spot. This result implies that most of the thermal pressure is maintained via the elastic resistance of the heated material, rather than through the constant volume restriction provided by the metal gasket.

Dewaele et al. [1998] performed finite element modeling – also based on solving the thermoelastic equations – for a realistic LHDAC model assembly consisting of samples

(stishovite and coesite) sandwiched between an argon pressure medium. Their analysis included the effects of the thermal conductivity of the sample and pressure medium on the temperature distribution, as well as the effects of the bulk and shear moduli parameterized as Lamé constants. For both coesite and stishovite, they differentiated between a model with solid and liquid argon as the pressure medium. Their results for a solid pressure medium compare well with the results cited by Heinz [1990] –a thermal pressure increase of ~30 % of the 'cold' pressure. Interestingly, they found only a small dependence of the thermal pressure on the relative amount of solid argon used as pressure medium. Their second model, assuming a completely molten pressure medium, reduced the expected thermal pressure by about 50 %. This model approached the free-surface model of Heinz [1990]. Importantly, Dewaele et al. [1998] also recognized the key role of deviatoric stresses generated by the thermal pressure exceeding the sample's shear strength in producing local (or, in the case of a fluid sample, sample-wide) anelastic relaxation of the thermal pressure. This shear strength-induced component represents a difficult-to-simulate effect on the thermal pressure distribution, and its uncertainty provides additional motivation for this experimental study.

Fiquet et al. [1996], for the first time, reported direct observations of thermal pressure in a LHDAC while measuring P-V-T data of MgO periclase using a CO_2 laser. Andrault et al. [1998] experimentally determined the pressure increase induced by laser heating in a LHDAC using the phase transitions in the Mg_2SiO_4 and SiO_2 systems. They found that the observed increase relative to the perfectly isochoric 'thermodynamic' limit is sample dependent, correlating positively with the product of the thermal expansion and bulk modulus, αK_T (in accord with the ideal thermodynamic definition of thermal pressure as equal to $\alpha K_T \mathrm{d}T$), rather than with the shear modulus. Kavner and Duffy [2001a] report a detailed analysis of P-T paths in a LHDAC based on energy-dispersive X-ray diffraction measurements and modelling calculations including hydrostatic pressure, temperature and deviatoric stresses. They show that P-T paths in a DAC are highly variable and can depend on details of sample preparation and loading, gasket material, pressure medium and even design details of the DAC itself. Furthermore, this study observes pressure relaxation upon prolonged heating that is ascribed to stress relaxation. Interestingly, such pressure drops were not observed in experiments where the sample had already undergone several heating and cooling cycles at the same spot. This study could not resolve any spatial pressure variation at high temperature due to thermal gradients because of both fundamental limitations of energy dispersive X-ray diffraction on one hand and the lack of 2-dimensional temperature information on the other hand. In this work, we experimentally quantify the distribution of thermal pressure created in a diamond anvil cell by a laser focus spot of 30 μm FWHM – a typical diameter of an experimental laser heating spot – and compare it with previously published models as well as a simple model based on the assumption of isochoric conditions. We then use an idealized example to quantify the effects of not fully taking into account the thermal pressure on thermoelastic properties of a mantle-like material ($Mg_{0.88}Fe_{0.12}SiO_3$ bridgmanite) extracted from a LHDAC experiment, and explore the implications for the resultant inferred mineralogy versus depth correlation.

2 Materials and Methods

We combine spatially resolved synchrotron X-ray powder diffraction [Kunz et al., 2005; Laugier and Bochu, 2002; Prescher and Prakapenka, 2015] at distributed points along a BX90 DAC's

sample chamber's diameter with a 2-dimensional temperature map [Kiefer and Duffy, 2005; Kunz et al., 2018; Manga and Jeanloz, 1996; Rainey and Kavner, 2014] of the sample chamber through pressure-volume-temperature (PVT) Murnaghan equation of states (EOS) [Anderson, 1997; Angel et al., 2014; Birch, 1952; Helffrich and Connolly, 2009; Murnaghan, 1951] on samples of AgI [Chauhan and Singh, 2007; Hull and Keen, 1999] and San Carlos olivine [Liu et al., 2005; Liu and Li, 2006] to determine the pressure distribution across the laser heated hotspot. By comparing these pressure values with the pressures measured at the same positions before the heating event, we obtain a distribution of the thermal pressure (P_{th}) produced by the heating event.

2.1 Samples

Experiments were performed on commercially available silver iodide, AgI (SIGMA-ALDRICH), and gem-quality San Carlos olivine, $[(Mg_{0.9}{}^{(2+)},Fe_{0.1}{}^{(2+)})_2\ SiO_4$. Table 1 shows each material's thermoelastic parameters as derived from the literature. Our choice of these two compounds is motivated both by each material having notably uniform and stable coupling with infrared laser heating, but also by the product of thermal expansion and bulk modulus (αK_0) of the two materials being almost equivalent (Table 1), while their strengths are expected to markedly differ. Accordingly, these two materials provide a means for experimentally demonstrating whether shear strength exercises a major role on thermal pressure, or whether thermal pressure is largely governed by the thermodynamics of local heating of a nearly isochoric system.

	AgI	San Carlos Olivine
Bulk Modulus (K_0)	42(2) GPa [(1)]	129.4(4) GPa [(2)]
dK/dP (K')	3.8(3) [(1)]	4.6(1) [(2)]
Thermal Expansion (α)	8 x 10^{-5}/K [(3)]	2.7(3) x 10^{-5}/K [(4)]
Anderson-Grüneisen Parameter (δ)	3.8(3)	4.6(1)
αK_0	3.36 x 10^{-3} GPa/K	3.49 x 10^{-3} GPa/K

Table 1: Thermoelastic parameters of AgI and San Carlos olivine at ambient pressure and temperature. (1) Hull and Keen [1999] (2) Liu et al. [2005], (3) The value for NaCl was used as an approximation Chauhan and Singh [2007], (4) Liu and Li [2006]. The Anderson-Grüneisen Parameter was set equal to dK/dP: this assumes that the isothermal derivative with respect to volume of αK_T is negligible, and represents a good approximation for both halides and olivine [Anderson, 1997].

The samples were powdered using a mortar and pestle, and X-ray powder diffraction of the samples at modest pressures (2 – 4 GPa) and room temperature confirmed their chemical purity. High pressures were generated using a BX90 diamond anvil cell [Kantor et al., 2012], with type 2a CVD diamonds (400 μm culets). Steel was used as the gasket material, which was pre-indented to a thickness of 100 μm, and laser drilled to yield sample chambers of 160 μm in diameter. Before loading, parallel tungsten blocks were used to compact the powdered samples.

To further reduce sample porosity, the gasket was loaded with the compacted sample, modestly pressurized (<3 GPa), and then loaded with more sample. Cold closing pressures were determined to be 6 GPa for the AgI, and 3 GPa for the San Carlos olivine using R-line fluorescence on a cluster of ruby chips [Mao et al., 1986] placed close to the center of the sample chamber.The samples were loaded without a pressure medium or thermal insulation material in order to keep artifacts due to insufficient geometric control of a multi-component sample assembly at a minimum. The lack of thermal insulation layers is justified in samples (like AgI and olivine) where the low thermal conductivity allows the sample in the center of the chamber to be robustly heated by the IR laser without draining its temperature through the diamond heat sinks. In essence, a thin sample layer in contact with the diamonds acts as the insulation layer for the bulk sample, and the sample itself therefore serves as its own thermal insulation layer. As shown by Manga and Jeanloz [1996], the axial temperature gradients expected in a dielectric material have a negligible effect on the temperature deduced from the observed thermal radiation spectrum. Furthermore, the lack of any observable peak broadening or splitting within the hot powder diffraction patterns indicates that the axial thermal gradients are very steep, and therefore the cold insulation layer is too thin to affect the diffraction patterns and thus bias the deduced thermal pressures.

2.2 Synchrotron X-ray Diffraction

Angle-dispersive in situ X-ray powder diffraction patterns at high pressure and high temperature were collected at beamline 12.2.2 [Kunz et al., 2005] at the Advanced Light Source at the Lawrence Berkeley National Laboratory using an X-ray wavelength of $\lambda = 0.5166$Å (24 keV) and $\lambda = 0.4969$Å (25 keV) for the silver iodide and San Carlos olivine experiments, respectively. The X-ray energy for the AgI was lowered to 24 keV to be at a safe distance from the Ag-K-α-absorption edge. At each spatial position, X-ray diffraction patterns were taken both before and during the IR laser heating to yield ambient and heated diffraction patterns. The X-ray beam size was 10 μm. Patterns were collected with exposure times of 30 secs on a MAR3450 image plate. The detector distance and orientation were calibrated using a CeO_2 standard at the sample position.

2.3 Laser Heating and Temperature Measurement:

Laser heating of the LHDAC was conducted using a 1090 nm IR fiber laser system [Kunz et al., 2018], with a beam size of 30 μm FWHM in diameter. The silver iodide sample was heated with $0.9 - 1.0$W in both the upstream and downstream directions, while the San Carlos olivine sample was heated with powers of $2.5 - 3.2$W upstream and $4.5 - 5.7$W downstream. To probe the sample across the hot spot, the sample had to be moved relative to the stationary X-ray beam, and with it, the laser hot spot which in turn was kept centered on the gasket hole (see Figure 1)

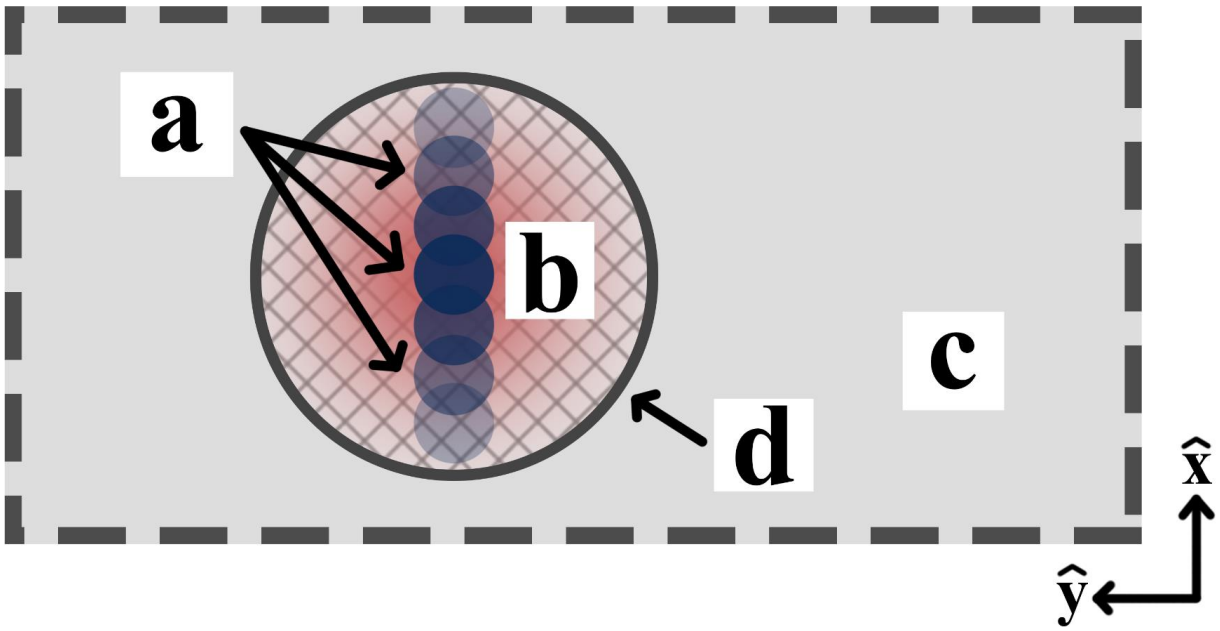

Figure 1: x-y cross section of the LHDAC as seen along the X-ray path. (A) X-ray beam positions (blue) across the diameter of the sample chamber. Note that the laser beam (red) is constantly centered at the origin of the sample space. (B) Portion of the heated powdered sample for which the temperature could be radiometrically measured. (C) Far-field of the sample material. (D) Border of the radiometrically-constrained area of the hot spot.

The center of the gasket hole served as the reference for positioning the laser hot spot. As a result, this procedure created an individual hot spot for every diffraction measurement. The laser heating set-up on beamline 12.2.2 [Kunz et al., 2018] allows for real-time temperature mapping of the sample chamber during a heating event. Temperatures were measured using the double sided spectroradiometric pyrometry set up on beamline 12.2.2, which employs a modified peak scaling approach [Rainey and Kavner, 2014]. This approach avoids the notorious chromatic aberration artifacts and also produces full absolute temperature maps in real time, thus enabling the spatial mapping of the thermal pressure effects presented here.

The pyrometry setup produces upstream and downstream 74 μm x 74 μm square temperature maps centered at the peak of the laser hotspot. As a result, radial temperature readings from the center of the sample exist from 0 to 37 μm for the full azimuthal range, but disregarding radial completeness, temperature data exist from 0 to 52.3 μm from the center. We plotted the upstream and downstream temperatures against radial distance by averaging the temperatures of pixels with the same Euclidian distance (within floating point error) from the center of the 74 μm x 74 μm temperature maps. The upstream and downstream results were averaged to produce an average temperature vs. radial distance plot. Due to the large thermal conductivity of the diamond anvils, it has been shown that at the diamond/sample interface, the sample has a temperature close to room temperature [Kiefer and Duffy, 2005]. The large thermal conductivity of the metallic gasket that is squeezed between the diamonds thus constrains the sample/gasket interface to be also close to room temperature in the situation where the laser hot spot is kept in the center of a gasket hole several times the size of the hot spot. To construct the

temperatures between 52.3 μm and 80 μm (the sample edge), we use a simple linear decrease between the points at $(44.5\ \mu m, \mathrm{avg}([T_{37\mu m}, T_{52.3\mu m}]))$ and $(80\ \mu m, 298K)$. To construct the first point of the linear decrease, we considered the temperature points between 37 μm and 52.3 μm because 360-degree azimuthal averaging is only possible between 0 and 37 μm. The average distance and temperature of the points between 37 μm and 52.3 μm gives us the starting point for the linear decrease.

The average temperatures of the area as probed by the 10 μm X-ray beam of sections centered between 0 and 47.3 μm (52.3 μm – 5 μm) was obtained by averaging the corresponding 10 μm section of the average temperature vs. radial distance graphs. Average beam temperatures of sections centered between 52.3 μm and 80 μm were obtained by taking the average temperature-value of the linear decrease over the corresponding 10 μm radial section. The resultant experimental temperature spots were then fit with a Gaussian function.

Errors in our temperature values were assessed as follows: We use the term "heating instance" to refer to the data generated by one heating at a fixed point. Each heating instance is associated with a numerical temperature (specified in Section 2.4) and a spatial coordinate. The peak temperatures for upstream and downstream measurements vary on average by ~150 *K*. We estimate the temperature error of each heating instance by setting their temperature variance to be 11250 K^2 (i.e. a variance accounting for a 150 *K* shift). This variance propagates to a final pressure standard error for the heating instance. Single points for the thermal pressure vs. radial distance plots in Figure 2 are an average of the heating instances at that spatial coordinate. To calculate the variance of this averaged pressure point, we assume that the heating instances are independent of one another, and as such the variances are additive.

2.4 Determination of Thermal Pressure:

We combine the Murnaghan Equation [Murnaghan, 1951] with the first order equation of thermal expansion through EosFit7 GUI [Angel et al., 2014] for the PVT EOS (*Equation 1*).

Equation 1

$$P = \frac{K_0(1+\alpha\Delta T)^{-\delta}}{K'}\left(\left(\frac{V_P}{V_0(1+\alpha\Delta T)}\right)^{-K'} - 1\right)$$

Within the pressure range and volumetric strains that we probe, the Murnaghan equation is expected to provide a valid representation of the pressure-volume behavior of these materials that is comparable in accuracy to other finite strain equations of state [e.g., [Birch, 1978]. Furthermore, the Murnaghan equation produces computational simplicity due to its straightforward invertability. The expanded Murnaghan equation (*Equation 1*) requires observable input values for the initial (V_0, before heating) and final (V_P, during heating) sample unit cell volumes, and the temperature change (ΔT) experienced by the probed sample volume, together with the physical constants K_0, K', α, and the Anderson-Grüneisen parameter δ [Angel et al., 2014; Helffrich and Connolly, 2009]. Note that in this formulation we account for the

temperature dependence of the bulk modulus through the Anderson-Grüneisen parameter δ, whereas no pressure or temperature dependence of the thermal expansivity α is included. This simple formulation of α reflects that the relative roles of pressure and temperature on this parameter are of opposite sign, and the effect of modest variations in thermal expansion on volume are dwarfed by the pressure effects observed. With V_0 and V_P determined using the unit cell parameters from before and during the laser-heating, and ΔT determined from the temperature map produced by the pyrometry set up on beamline 12.2.2, *Equation 1* yields the total pressure at every position of the X-ray/sample transect (Figure 1). To obtain the thermal pressure component P_{th}, we subtract the pressure obtained through Equation 1 at the corresponding position prior to the heating from that calculated at high temperatures (i.e. we subtract the pressure applied by the diamonds at ambient temperature). Note that the cold pressures determined from data taken before and after heating were identical.

Scattering intensity versus 2θ plots were obtained by azimuthal integration of the 2-dimensional powder diffraction patterns using DIOPTAS [Prescher and Prakapenka, 2015]. From the intensity versus 2θ plots for the silver iodide sample, lattice spacings with Miller indices (200), (220), (311), (222), (400), (420), and (422) were used to refine the unit-cell parameters of silver iodide's cubic crystal structure. From the intensity versus 2θ plots for the San Carlos olivine, lattice spacings with Miller indices (020), (021), (101), (002), (130), (131), (112), and (211) were analyzed using Celref 3 [Laugier and Bochu, 2002] to yield orthorhombic unit-cell parameters.

As an ancillary experimental aspect, we note that the temperatures in our experiments are such that Soret diffusion of iron in olivine is not expected to affect our results. The characteristic e-folding time-frame for Soret diffusion to converge on a steady-state chemical distribution in a constant thermal gradient can be approximated by $\theta = h^2/\pi D_{Fe\text{-}Mg}$, where h is the characteristic sample length-scale, and $D_{Fe\text{-}Mg}$ is the inter-diffusion coefficient of iron and magnesium in olivine [Allnatt and Chadwick, 1967]. At ~1500 K (our peak temperature) and 4 GPa, the value of $D_{Fe\text{-}Mg}$ of olivine is ~2 x 10^{-15} m^2/sec [Farber et al., 2000]); the temperature dependence of the diffusion rate is such that it decreases by about 5 orders of magnitude as temperature is lowered to 950 K [Dohmen et al., 2007]. Using just the highest temperature of our experiments, and an effective radius of the hotter portion of our spot of 25 μm, we derive a net e-folding time for Soret diffusion of ~10^5 seconds: given that we are utilizing our highest temperature, and spatially averaged diffusion rates are hence much lower, this time-frame represents a *substantial* underestimate. Therefore, given that our measurement durations are of order 10^2-10^3 seconds, Soret diffusion will almost certainly not impact our experiments.

2.5 Formulation of a simple model for P_{th}:

We limit our examination to the thermal pressure arising due to restrictions on the total volume. The construction of our model is as follows:

We reduce the sample chamber to a circular geometry, which we can then partition with shell differential elements. Consider the thermal pressure that arises at the differential element r (i.e. the region in the radial interval $[r - dr, r + dr]$). Considering this element consequently

divides the entire sample into two regions: the interior – the region within the radial interval $[0, r - dr]$, and the exterior – the region within the radial interval $[r + dr, b]$ (where b is the radius of the entire sample).

Predicated on Heinz [1990] analysis and consistent with the intensity of the heating laser, we approximate the temperature distribution with a Gaussian curve. As such, when we move farther away from the center of the sample, the temperature decreases. Thus, the thermal expansion in the hotter interior region $[0, r - dr]$ is greater than that of the cooler exterior region $[r + dr, b]$. If we hold the volume of the interior region constant, thermal pressure arises to counteract this thermal expansion as dictated by the volumetric restriction. Similarly, holding the volume of the exterior region constant results in a smaller thermal pressure relative to that in the interior. The constant volume restriction allows us to think of the *r*-shell as being incompressible – which translates to a direct analogy with infinite shear strength of the sample. With this construction, the *r*-shell experiences a greater thermal pressure from the thermal expansion of the interior volume (which points radially outwards at the boundary $r - dr$) than the thermal pressure it experiences from the exterior (which points radially inwards at the boundary $r + dr$). Of course, in reality as $dr \to 0$, the greater interior thermal pressure would cause the interior volume to expand and thus equilibrate with the outer volume. However, modeling thermal pressure by isochorically restricting the interior volume represents a reasonable upper bound.

With this framework in mind, we can derive a mathematical model. As mentioned above, we use a Gaussian curve to model the temperature distribution of the heated sample (*Equation 2*).

Equation 2

$$T(x) = T_0 + \left(\frac{A}{w\sqrt{\pi/2}}\right) \exp\left(-2\left(\frac{x - x_c}{w}\right)^2\right)$$

Note that *Equation 2* is the area version of the Gaussian Equation.

In *Equation 2*, x_c denotes the center of the curve (i.e. at x_c, $T(x_c)$ has its maximum), *A* denotes the area under the curve on the interval $[x_c - \sigma, x_c + \sigma]$, and *w* denotes the width of the curve on the interval $[x_c - \sigma, x_c + \sigma]$, which is 2σ.

Using the area version of the Gaussian function lets us fit our temperature data with the Levenberg-Marquardt iteration algorithm. With temperature expressed as a function of radius, we can express the thermal expansion coefficient and the bulk modulus as functions of temperature. For the thermal expansion coefficient, we use Equation 3 as a simplified formulation

Equation 3

$$\alpha(r) = \alpha_0 + \alpha_1 T(r)$$

For the bulk modulus, we introduce the Anderson-Grüneisen parameter to link compressibility with thermal expansion (Equation 4).

Equation 4

$$K(r) = K_0\left(1 + \alpha(r)\Delta T(r)\right)^{-\delta}$$

In the following derivation of the bulk modulus as a function of radius, dV_0 represents the volume of the unheated shell (i.e. the radial interval $[r - dr, r + dr]$) and dV_T represents the thermally expanded segment of dV_0 under unconstrained conditions

Equation 5

$$K(dV_T) = K_0\left(\frac{dV_0}{dV_T}\right)^{\delta}$$

Equation 6

$$K(r) = K_0\left(\frac{dV_0}{dV_0(1 + \alpha(r)\Delta T(r))}\right)^{\delta}$$

For a given *r*-shell, the interior region expands to some heated volume, and the sum of the thermal expansion of the heated interior shells (i.e. $\int_0^r dV_T$) is pressurized to match the isochoric assumption of the interior volume (i.e. $\int_0^r dV_P = \pi r^2$). We employ the equation for the thermal expansion to represent the volumetric expansion of each interior shell (i.e. $dV_T = dV_0\big(1 + \alpha(r)\Delta T(r)\big)$), and we use the Murnaghan equation (*Equation 1*) to model the pressure needed to compress the sum of the heated volumes to adhere to the isochoric restriction (Equation 7, Equation 8, Equation 9).

Equation 7

$$dV_P = dV_T\left(1 + \frac{K'}{K}P\right)^{-\frac{1}{K'}}$$

Equation 8

$$\pi r^2 = \int_r^0 dV_T\left(1 + \frac{K'}{K}P\right)^{-\frac{1}{K'}}$$

Equation 9

$$\pi r^2 = \int_0^r 2\pi x dx\big(1 + a(x)T(x)\big)\left(1 + \frac{K'}{K(x)}P_{th}\right)^{-\frac{1}{K'}}$$

Thus, Equation 9 presents an upper bound for the thermal pressure that arises at a radial distance *r*. Note that due to the steepness of the Gaussian temperature curve in our experiments, the thermal pressure of the interior region dominates the thermal pressure contribution at a given radius, so taking our upper bound results in a good estimate for the real thermal pressure.

3 Data

3.1 Temperature Profiles:

Figure 2 shows the temperature profile (red) across the hot spots in AgI and San Carlos olivine. The hot-spots can be fit with a Gaussian function, and have approximately the width of the laser spot. These are in agreement with the Gaussian intensity distribution of the IR fiber laser, and indicate that the coupling of the samples with the laser is not markedly temperature dependent. Both temperature curves decrease to basically room temperature at the sample/gasket interface. This confirms the highly local nature of the temperature distribution in laser-heated samples within a DAC. It is therefore justified to assume that the cold gasket does not suffer any temperature-induced deformation: indeed, no irreversible deformation, as manifested by a shift

in sample diameter, was observed following heating. The heating process of the entire sample volume is thus, to a first approximation, isochoric. To second order, it is possible that localized heating of the anvils may produce a slight contraction in the axial direction of the sample (even while the radial direction remains unchanged): the trade-off between the elastic response of the anvil to the thermal pressure within the sample and the thermal pressure induced by localized heating is difficult to characterize, but this effect is likely to be small. Indeed, the lack of irreversible sample deformation or significant pressure relaxation following heating supports the largely isochoric character of these samples, and hence the lack of relaxation of the thermal pressure over the course of the experiment. Moreover, the pressures of the samples are sufficiently low that deviatoric stresses are not significant: hence, our results are unlikely to be affected by local stress relaxation [Kavner and Duffy, 2001a]. Comparig the temperature profile with the melting line of AgI [Ohtaka et al., 2002] linearly extrapolated to the total peak pressure of about 9 GPa indicates that the peak temperature in the AgI experiment was very close to the melting line. The persistence of the diffraction peaks, however, indicate that the material was still in its crystalline rock-salt structured phase.

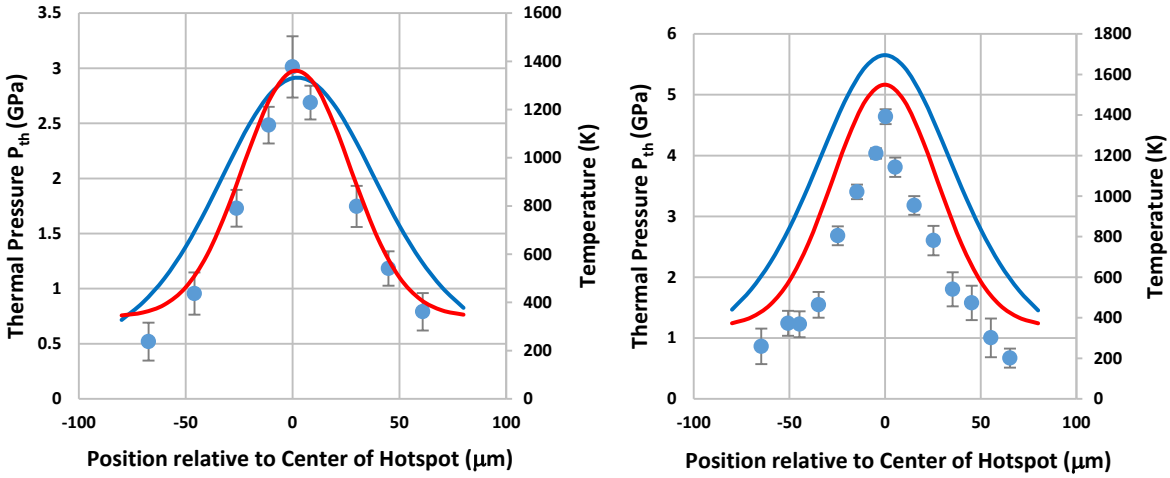

(a) (b)

Figure 2: Observed beam temperature across the hotspot (red) and observed (blue symbols) and modeled (blue line) thermal pressure in AgI (a) and San Carlos olivine (b). The position of the pressure peak coincides with the hotspot peak as is expected for a thermal pressure-induced increase. Notably, any spatial averaging associated with the size of our X-ray probe (~10 μm) relative to the size of the hotspot will produce an underestimate of the thermal pressure above the half-maximum of the thermal pressure distribution.

3.2 Pressure Profiles:

Figure 2 also shows the observed thermal pressure distribution (blue dots) across the laser heated hotspot (red line) as calculated from the procedure described in Section 2.4 using the thermoelastic constants given in Table 1.

In both samples, a significant pressure peak, at the same location as the peak of the hotspot, is observed. In AgI, we observe a maximum thermal pressure of ~ 3 GPa at the center of the hotspot (~1400 K). It decreases to 0.5 GPa within about 70 μm. At the steepest part of the slope, about 20 μm from the center, the pressure drops by about 0.4 GPa per 10 μm. In San Carlos olivine, the situation is similar. A pronounced pressure maximum of ~4.5 GPa above the room-temperature value is measured at the center of the hotspot (~1600 K). The thermal gradient is somewhat larger than in AgI, ~1 GPa/10 μm: this difference likely reflects the marked difference in strength between the two materials. It is notable, however, that even within a weak solid like AgI, the thermal pressure remains localized and does not fully re-equilibrate through viscous relaxation across the sample over the multi-minute course of the experiment.

Indeed, in both materials the thermal pressure distribution closely traces the temperature distribution, giving testament to the local nature of thermal pressure as predicted by Dewaele et al. [1998] and Heinz [1990]. Nevertheless, an effect that is plausibly associated with material strength can be experimentally discerned: the peak thermal pressure in AgI is slightly lower and the pressure distribution is wider than is observed in olivine.

4 Results

This is – to the best of our knowledge – the first documented experimental determination of the spatial distribution of thermal pressure across a laser heated spot within the diamond anvil cell. The general magnitude of the values reported here correspond quite well to the thermodynamic thermal pressure ($\alpha K_0 \, \mathrm{d}T$) and also agree well with values predicted by Heinz [1990] for his constant volume model. That model corresponds closely to our experimental arrangement where a sample is loaded without pressure medium into a DAC and heated locally with a hot spot that is notably smaller than the sample diameter. As expected, our values are somewhat higher (when adjusted for the hotspot's peak temperature) than the thermal pressures predicted by Dewaele et al. [1998] using finite element modeling. This is due to the fact that their modelling set-up included solid or liquid argon surrounding the sample as a pressure transmitting medium: such rare gas media are expected to be weak at high pressures (and temperatures), although argon can maintain substantial pressure gradients above ~20 GPa at 300 K [Klotz et al., 2009].

The local nature of the observed thermal pressure is due to the finite shear strength of the expanding sample in a constrained volume. If the heated sample were a liquid or melt with no shear strength, the thermal pressure would equilibrate over the entire gasket hole. For the materials, the size of the heated spot and sample, and the peak temperatures considered in this study, the equilibrated thermal pressure would amount to a homogeneous ~1.25 – 1.5 GPa increase across the entire sample volume. The observed gradients in thermal pressure therefore confirm that the temperatures attained were well below the melting point: however, even within a material that is expected to be relatively weak (AgI), localized thermal pressure-induced pressure increases of several GPa are observed.

The predicted pressure distributions of our simple model described in Section 2.5 (blue curve) are compared with the experimental data (blue dots) in Figure 2. For AgI, the model predicts the peak pressure accurately, but under-estimates the pressure gradient. In the case of San Carlos olivine, the model predicts a pressure distribution that is shifted upward from the observed values by about 1 GPa (at an observed peak pressure of ~ 4.5 GPa). We attribute this discrepancy to the pressure gradient being too steep to be resolved with a 10 μm sized X-ray spot, thus biasing the measured pressures towards lower values. This is consistent with the fact that the model matches the measured values much better for AgI where the lower shear strength allows for a flatter pressure gradient, which is better matched to the 10 μm X-ray spot size used. We therefore expect the real pressure increase within olivine to be larger and to lie between the measured spots and the values given by the model.

Our measurements demonstrate that even for soft materials at temperatures close to their melting line, like AgI [Ohtaka et al., 2002], a significant pressure increase coupled with a pressure gradient around the localized hot spot is maintained in laser-heated diamond anvil cells. Given the steepness of the observed pressure gradient, this thermally-induced pressure increase and gradient is also expected to be significant in samples that are embedded in 'soft' pressure media such as Ne or He where their shear strength at high pressures becomes sufficient to contain the thermal pressure within the embedded sample (e.g. Klotz et al. [2009]). The shear strengths of the media consequently negate the full pressure-equilibrating effect expected in hydrostatic media for pressures generated locally in the sample through spot laser heating. These findings have ramifications for the design and interpretation of in-situ high-pressure high-temperature diffraction studies aimed at determining PVT equations of state of Earth materials and consequently for the mineralogical interpretation of geophysical density profiles based on LHDAC results.

Ramifications for LHDAC experimental designs:

(1) If, during a LHDAC experiment, pressure is measured before and after the heating event, pressure can be significantly underestimated in the center of the hotspot (i.e. where the X-rays usually probe the sample) during the heating event: such localized, thermally-induced pressurization has not been previously characterized (e.g. Andrault et al. [1998]; Kavner and Duffy [2001b]).

(2) Pressure measurements using the diffraction lines of a temperature-insulating pressure medium (i.e. Ne, Ar, He) may similarly underestimate the pressure within the hot sample given the steep pressure gradients we observed within the hotspot. The underestimation of the pressure derived from the lattice parameters of a solid, non-laser-absorbing pressure medium (such as NaCl or MgO) could be larger if the pressure medium simultaneously also acts as a thermal insulation material shielding the diamonds from the laser hot spot. In the particular case of a particularly thick thermally insulating medium, it is possible that a significant portion of the diffracting volume within the pressure medium may be at a temperature significantly below the peak temperature.

(3) As a consequence of (1) and (2), the most reliable pressure determination in a laser heated diamond anvil cell is likely generated by a pressure standard that is intimately mixed with the sample, monitored in situ at simultaneous high temperature and pressure,

and which differs from the material used to thermally insulate the diamonds from the sample. Ideally, such an internal calibrant (often Pt) would also be chemically inert at extreme conditions in order to avoid unwanted chemical reaction or alloying with the sample. Indeed, such a mixed phase geometry can be particularly effective when deployed in instances where the calibrant itself is used as the laser-absorber within the sample (e.g. Tateno et al. [2019]).

(4) The observed steep gradients in thermal pressure demonstrate that a straightforward means of experimental optimization, in terms of sampling a spot at a well-constrained pressure and temperature, is to combine a large uniform hot spot (which can be generated using beam shaping optics, such as a Pi shaper) with the smallest possible X-ray probe. Naturally, a small X-ray beam has the inherent problem of reduced data quality due to a decrease in powder statistics. This is especially true at high temperatures where recrystallization and grain growth are often observed (e.g. [Irifune et al., 2005] , [Shen et al., 1998]). While poor powder diffraction statistics might still allow extraction of reliable volumetric data, other approaches could involve dispensing with monochromatic powder diffraction for PVT equation of state determinations based on diffraction. Single crystal and multigrain diffraction techniques are obvious alternatives that are commonly deployed at ambient temperatures, but are difficult (although not in principle impossible) to combine with laser heating, due to the requirement that the sample be rotated relative to the X-ray beam [Dubrovinsky et al., 2010]. X-ray Laue microdiffraction can be a useful tool in cases where a sample cannot easily be rotated as required on a monochromatic single crystal diffractometer (e.g. Barkov et al. [2019]; Tamura et al. [2002]). However, in the absence of energy resolving area detectors, the application of Laue microdiffraction to PVT equation of state studies (where accurate sizes of unit cells are determined) is not practical. A potentially viable technique that can be deployed using commonly available equipment is energy resolved Laue diffraction, which can use a scanning monochromator rather than an energy resolving detector. To make this approach feasible in the traditional transmission geometry employed in laser heating set-ups (e.g. Kunz et al. [2018], Shen et al. [2001]) requires a very large energy range (~ 15 keV < E < 50 keV) to be covered in order to overcome the low density in reciprocal space coverage at low diffraction angles (e.g. Kunz et al. [2009]). Alternatively, a set-up where the laser heating is in the axial direction through the diamonds, but the detector is positioned at 90 degrees (i.e. signal through X-ray transparent gasket) could be envisaged.

The key point here is that the sharply peaked pressure distributions that we document within laser-heated spots motivate either smaller X-ray probes (and larger heated spots) than have previously been typically deployed, or alternate diffraction techniques to enhance the spatial resolution of the X-ray probe itself.

Ramifications for geophysical models derived based on LHDAC experiments:

A systematic off-set in the assumed pressures for PVT equation of states, as would occur if part of the induced thermal pressure is not recognized, has consequences for the geophysical conclusions deduced from such experiments. As an example, we tested the effect on a

hypothetical experiment on bridgmanite ($Mg_{(1-x)}Fe_xSiO_3$ (x = 0.12)). We created a synthetic PVT dataset with pre-heated pressures between ~25 and 100 GPa and 3 different mantle relevant temperatures (1700, 2200 and 2700 K), with imposed thermoelastic parameters (V_0, K_0, K', Anderson-Grüneisen δ, α_0, dα/dP) derived from the literature and tabulated in Table 2. We add to the pre-heated pressure a thermal pressure of $\alpha K \Delta T$ (~ 12 GPa, assuming an αK ~ 5 x 10^{-3} GPa/K) in accordance with our measurements. We then use these synthetic V/V_0 – T data to fit a Murnaghan equation of state by assuming pressures that underestimated the total pressure by 2 GPa (a conservative assumption that involves missing only a small part of the potential total thermal pressure of 12 GPa). For numerical convenience and consistency with our approach, weemploy the Murnaghan equation here, instead of for example the Birch-Murnaghan formalism, which is somewhat better suited for the pressure range considered in this example. This choice of equation of state may introduce minor deviations in the absolute pressures modeled, but those will not affect the conclusions derived which rely on relative pressure changes associated with thermal pressure.

This process yields a set of thermoelastic properties that are biased through the neglect of even this small component of thermal pressure (Table 2). As can be seen from Table 2, both the Anderson-Grüneisen parameter δ, (dK/dT) and dα/dP refine towards values that predict a density vs pressure curve that is shifted positively (to higher densities) relative to the true values (Figure 3). If such a slightly overestimated density vs depth (i.e. P and T) profile were compared with seismic data to, for example, estimate the Fe content in bridgmanite in the Earth's mantle, this density difference would lead to an underestimate of the Fe content in the deep mantle. For our model parameters, the sensitivity of the system is such that even this small neglect of thermal pressure would generate an underestimate of the deep mantle's inferred Fe number (based on a too-dense EOS) of ~0.03.

	"Synthetic" values	Refined values
V_0 (Å^3)	163.7[1)]	Not refined
K_0 (GPa)	246.7[1)]	230.2(5)
K'	4.03[1)]	4.40(1)
Anderson-Grüneisen δ	3.25[2)]	1.74(6)
α_0 (K^{-1})	2.0 x 10^{-5} [3)]	1.63(2) x 10^{-5}
dα/dP ($K^{-1}GPa^{-1}$)	-1.0 x 10^{-7} [3)]	-1.01(2) x 10^{-7}

570

571 *Table 2: Thermoelastic parameters for the "synthetic" bridgmanite that were used to create*
572 *ideal V/Vo(P,T) values together with the corresponding values obtained from fitting a*
573 *Murnaghan equation against the same V/V_0 and temperature values, but pressure points that are*
574 *systematically underestimated by 2 GPa. The total thermal pressure was assumed to be equal to*
575 *12 GPa. See text for more details. 1) Shukla et al. [2016]; 2) The 'synthetic' δ is estimated by*
576 *equating $K_0 + dK/dT \times \Delta T = K_0 \times [1 + \alpha(P) \times \Delta(T)]^{-\delta}$ and solving for δ. A dK/dT of ~ -0.01*
577 GPa/K is assumed [Shukla et al., 2016]), and α(P) is assumed to be ~ 1.6 x 10^{-5}/K (Wang et al.
578 [1994]; Utsumi et al. [1995])

579

580

581

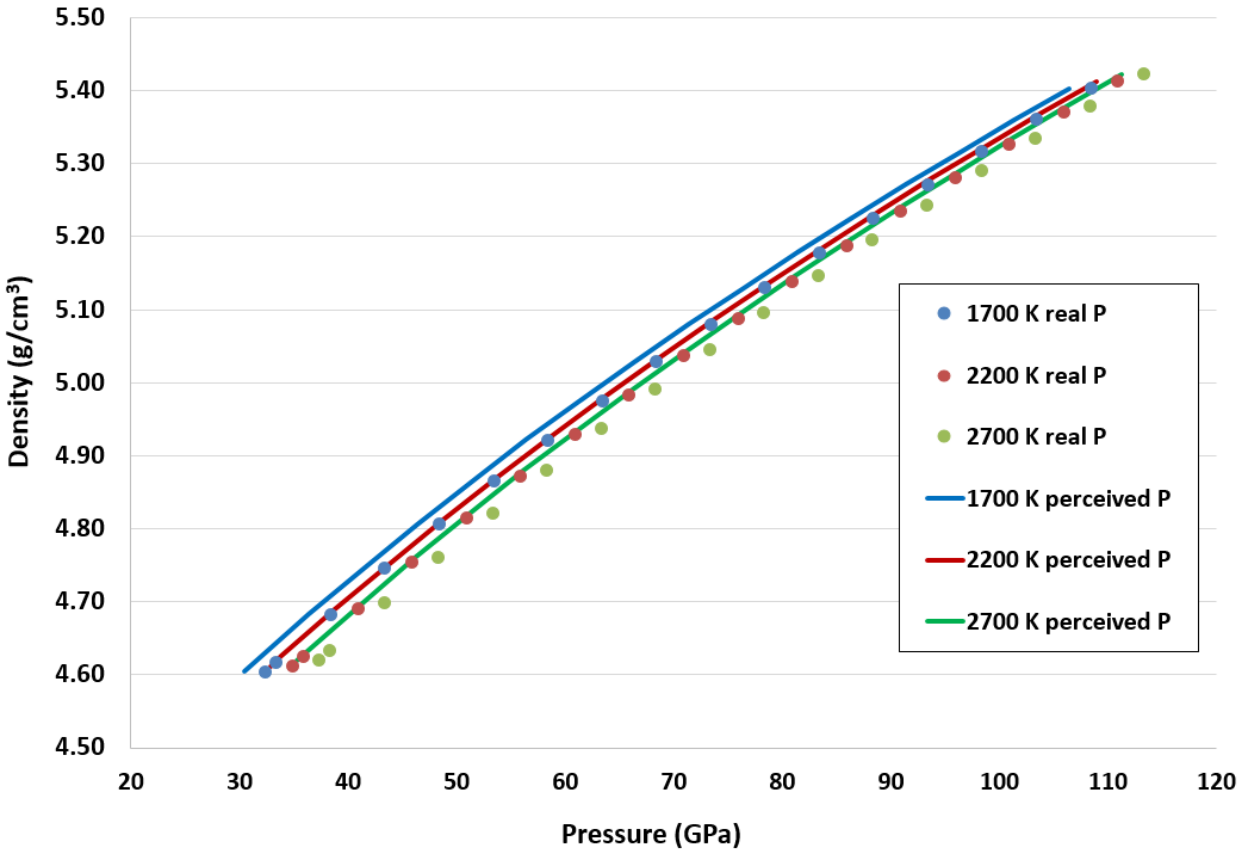

582

583 *Figure 3: Density versus pressure values for synthetic ideal $(Mg_{0.88}Fe_{0.12})SiO_3$ bridgmanite and*
584 *curves derived from thermoelatic properties as obtained from a PVT data set that*
585 *underestimated a total thermal pressure of 12 GPa by 2 GPa. Even this minor difference can*
586 *lead to a significant underestimate of the Fe content of bridgmanite in the deep mantle (see text).*

We note also that the localization of the thermal pressure elevations that we observe (Figure 2) suggests possible experimental avenues to measure difficult-to-characterize thermodynamic derivative properties. In particular, the sample translation techniques that we have documented can be deployed to measure the thermal pressure distributions within specially designed sample configurations. In particular, as shown in Supporting Information Section 1, for a sample suspended in a medium that is of extremely high rigidity (diamond is a logical candidate), the change in thermal pressure should entirely reflect the thermodynamic value of $\alpha K_T \, dT$. As such, if the thermal pressure can be assessed at two (or more) different pressures at high temperatures, the thermodynamic relation of αK_T (at P,T) - αK_T (at P_0, T) being equal to the volumetric integral of $(\delta_T - K'_T)dlnV$ can be deployed to provide a direct measure (assuming K' is constrained from equation of state measurements) of the Anderson-Grüneisen parameter at extreme conditions (e.g., Anderson and Isaak [1993]; Jackson and Rigden [1996]). The Anderson-Grüneisen parameter, which dictates the volume dependence of thermal expansion, is difficult to constrain at high pressures: it is inferred to decrease with compression, but its pressure dependence is not well known (Anderson and Isaak [1993]). In passing, we note that the other end-member, measurement of thermal pressure within a medium with zero strength (and high gasket strength), could also be deployed to constrain the pressure dependence of thermal pressure. In this instance, an accurate characterization of both the volume of the heated sample and of the sample chamber as a whole would be required to accurately interpret the sample-wide thermal pressure increase. Hence, our present measurements demonstrate that, with appropriate experimental designs, accurate constraints on the pressure-dependence of the Anderson-Grüneisen parameter could be generated from thermal pressure characterizations.

5 Conclusions

For the first time, we present a quantitative experimental characterization of the pressure gradients caused by thermal pressures induced by temperature gradients in the laser-heated diamond anvil cell. The observed pressure increases correspond in magnitude to previously published theoretical and modeled values, and are also in accord with the thermodynamically expected value: the dominant parameter that governs the magnitude of thermal pressure is, unsurprisingly, the product of thermal expansion and the bulk modulus. Our results indicate that there is a nuanced effect on thermal pressure associated with material strength in solid media, thus showing that some diffusion of the stress field occurs within the samples. In particular, our results on AgI are both lower in their peak thermal pressure and have smaller spatial gradients of pressure with distance, which is consistent with AgI being weaker than olivine. Our simple modeling overestimates the thermal pressures accessed by olivine. We attribute this to our model providing an upper limit on the thermal pressure, coupled with the size of our X-ray probe being relatively large (10 μm) compared to the steepness of the pressure gradients (this is especially acute in olivine, where the observed pressure gradients are ~1 GPa/10 μm).

From an overarching perspective, our results clearly demonstrate that thermal pressures within laser-heated spots can be substantial and, even within relatively weak materials (AgI), remain localized around the laser-heated hot spot. As such, high-pressure/high-temperature measurements of (particularly) derivative parameters, such as thermal expansion at high pressures, likely require either multiple internal standards and/or a liquid medium to ensure that

thermal expansions at extreme conditions are not underestimated. We also show that only a partial neglect of the thermal pressure can result in errors of the derived thermoelastic properties that lead towards inferred higher density at a given P and T conditions. This in turn can cause significant errors on the correlation between density and mineralogy, and could lead to an underestimate of the iron content of the deep mantle. Finally, our experimental design for measuring the spatial variations of thermal pressure could be deployed to quantitatively measure the pressure dependence of thermal pressure, and hence provide a direct constraint on the variation in the Anderson-Grüneisen parameter at deep planetary conditions.

Acknowledgments, Samples, and Data

All raw data and analysis (diffraction images, temperature maps, pressure calculations, and dynamic model graphs) are deposited in Dryad data repository (https://doi.org/10.7941/D1F63W, during review period:
https://datadryad.org/stash/share/42ALf7uVC5rr_RYU2bVkpACzuS0yjK1YKpVR8fjod6k).

X-ray diffraction experiments were performed at ALS beamline 12.2.2. We thank the Advanced Light Source (ALS), which is supported by the Director, Office of Science, Office of Basic Energy Sciences, Materials Sciences Division, of the US Department of Energy under Contract No. DE-AC03-76SF00098 at the Lawrence Berkeley National Laboratory and the University of California, Berkeley. Parts of the experimental work (sample preparation) benefitted from the ALS laser mill purchased by the Consortium for Materials Properties Research in Earth Sciences; COMPRES supported this project under the NSF Cooperative Agreement EAR 16-49658. QW is supported by NSF EAR-1620423. EY was supported by the private funding (Yen-Zantua).
Discussions with Dion Heinz greatly improved this manuscript and are warmly acknowledged. A special thanks is owed to Howard Padmore who not only helped fund this project, but also acted as a mentor and source of inspiration.
The authors contributed to the work as follows: Conceptualization: MK, QW; Investigation: CEY, MK; Data Curation: CEY; Methodology: CEY, MK; Formal Analysis: CEY; Software: CEY; Validation: CEY, QW, MK; Writing – original draft: QEY; Writing Review & Editing: MK, QW, CEY; Resources: MK, QW; Supervision: MK.
None of the authors as any conflict of interest to report.

References

Allnatt, A., and A. Chadwick (1967), Thermal diffusion in crystalline solids, *Chemical Reviews*, *67*(6), 681-705.

Anderson, O. L. (1997), The volume dependence of thermal pressure in solids, *Journal of Physics and Chemistry of solids*, *58*(2), 335-343.

Anderson, O. L., and D. G. Isaak (1993), The dependence of the Anderson-Grüneisen parameter δT upon compression at extreme conditions, *Journal of Physics and Chemistry of Solids*, *54*(2), 221-227.

Andrault, D., and G. Fiquet (2001), Synchrotron radiation and laser heating in a diamond anvil cell, *Review of Scientific Instruments*, *72*(2), 1283-1288.

Andrault, D., G. Fiquet, J.-P. Itie, P. Richet, P. Gillet, D. Haeusermann, and M. Hanfland (1998), Thermal pressure in the laser-heated diamond-anvil cell; an X-ray diffraction study, *European Journal of Mineralogy*, *10*(5), 931-940.

Angel, R. J., M. Alvaro, and J. Gonzalez-Platas (2014), EosFit7c and a Fortran module (library) for equation of state calculations, *Zeitschrift für Kristallographie-Crystalline Materials*, *229*(5), 405-419.

Barkov, A. Y., L. Bindi, N. Tamura, G. I. Shvedov, B. Winkler, C. V. Stan, W. Morgenroth, R. F. Martin, F. Zaccarini, and C. J. Stanley (2019), Ognitite, NiBiTe, a new mineral species, and Co-rich maucherite from the Ognit ultramafic complex, Eastern Sayans, Russia, *Mineralogical Magazine*, *83*(5), 695-703.

Bassett, W. A. (2016), Diamond Anvil Cells: Laser Heating of Samples at High Pressure: 50 Years, *Laser Focus World*.

Birch, F. (1952), Elasticity and constitution of the Earth's interior, *Journal of Geophysical Research*, *57*(2), 227-286.

Birch, F. (1978), Finite strain isotherm and velocities for single-crystal and polycrystalline NaCl at high pressures and 300 K, *Journal of Geophysical Research: Solid Earth*, *83*(B3), 1257-1268.

Chauhan, R., and C. Singh (2007), Equation of state and thermal expansivity of NaCl under high pressure and high temperature, *Physica B: Condensed Matter*, *387*(1-2), 352-357.

Dewaele, A., G. Fiquet, and P. Gillet (1998), Temperature and pressure distribution in the laser-heated diamond–anvil cell, *Review of scientific instruments*, *69*(6), 2421-2426.

Dohmen, R., H.-W. Becker, and S. Chakraborty (2007), Fe–Mg diffusion in olivine I: experimental determination between 700 and 1,200 C as a function of composition, crystal orientation and oxygen fugacity, *Physics and Chemistry of Minerals*, *34*(6), 389-407.

Dorogokupets, P., A. Dymshits, T. Sokolova, B. Danilov, and K. Litasov (2015), The equations of state of forsterite, wadsleyite, ringwoodite, akimotoite, MgSiO3-perovskite, and postperovskite and phase diagram for the Mg2SiO4 system at pressures of up to 130 GPa, *Russian Geology and Geophysics*, *56*(1-2), 172-189.

Dubrovinsky, L., T. Boffa-Ballaran, K. Glazyrin, A. Kurnosov, D. Frost, M. Merlini, M. Hanfland, V. Prakapenka, P. Schouwink, and T. Pippinger (2010), Single-crystal X-ray diffraction at megabar pressures and temperatures of thousands of degrees, *High Pressure Research*, *30*(4), 620-633.

Farber, D. L., Q. Williams, and F. J. Ryerson (2000), Divalent cation diffusion in Mg2SiO4 spinel (ringwoodite), β phase (wadsleyite), and olivine: Implications for the electrical conductivity of the mantle, *Journal of Geophysical Research: Solid Earth*, *105*(B1), 513-529.

Fiquet, G., D. Andrault, A. Dewaele, T. Charpin, M. Kunz, and D. Häusermann (1998), PVT equation of state of MgSiO3 perovskite, *Physics of the Earth and Planetary Interiors*, *105*(1-2), 21-31.

Fiquet, G., D. Andrault, J. Itie, P. Gillet, and P. Richet (1996), X-ray diffraction of periclase in a laser-heated diamond-anvil cell, *Physics of the Earth and Planetary Interiors*, *95*(1-2), 1-17.

Heinz, D. L. (1990), Thermal pressure in the laser-heated diamond anvil cell, *Geophysical Research Letters*, *17*(8), 1161-1164.

Helffrich, G., and J. Connolly (2009), Physical contradictions and remedies using simple polythermal equations of state, *American Mineralogist*, *94*(11-12), 1616-1619.

Hull, S., and D. Keen (1999), Pressure-induced phase transitions in AgCl, AgBr, and AgI, *Physical Review B*, *59*(2), 750.

729 Irifune, T., M. Isshiki, and S. Sakamoto (2005), Transmission electron microscope observation of the high-pressure
730 form of magnesite retrieved from laser heated diamond anvil cell, *Earth and Planetary Science Letters*, *239*(1-2),
731 98-105.
732
733 Ismailova, L., E. Bykova, M. Bykov, V. Cerantola, C. McCammon, T. B. Ballaran, A. Bobrov, R. Sinmyo, N.
734 Dubrovinskaia, and K. Glazyrin (2016), Stability of Fe, Al-bearing bridgmanite in the lower mantle and synthesis of
735 pure Fe-bridgmanite, *Science advances*, *2*(7), e1600427.
736
737 Jackson, I., and S. M. Rigden (1996), Analysis of PVT data: constraints on the thermoelastic properties of high-
738 pressure minerals, *Physics of the earth and planetary interiors*, *96*(2-3), 85-112.
739
740 Kantor, I., V. Prakapenka, A. Kantor, P. Dera, A. Kurnosov, S. Sinogeikin, N. Dubrovinskaia, and L. Dubrovinsky
741 (2012), BX90: A new diamond anvil cell design for X-ray diffraction and optical measurements, *Review of Scientific*
742 *Instruments*, *83*(12), 125102.
743
744 Kavner, A., and T. S. Duffy (2001a), Pressure–volume–temperature paths in the laser-heated diamond anvil cell,
745 *Journal of Applied Physics*, *89*(3), 1907-1914.
746
747 Kavner, A., and T. S. Duffy (2001b), Strength and elasticity of ringwoodite at upper mantle pressures, *Geophysical*
748 *Research Letters*, *28*(14), 2691-2694.
749
750 Kavner, A., and C. Nugent (2008), Precise measurements of radial temperature gradients in the laser-heated
751 diamond anvil cell, *Review of Scientific Instruments*, *79*(2), 024902.
752
753 Kiefer, B., and T. S. Duffy (2005), Finite element simulations of the laser-heated diamond-anvil cell, *Journal of*
754 *Applied Physics*, *97*(11), 114902.
755
756 Klotz, S., J. Chervin, P. Munsch, and G. Le Marchand (2009), Hydrostatic limits of 11 pressure transmitting media,
757 *Journal of Physics D: Applied Physics*, *42*(7), 075413.
758
759 Komabayashi, T., and Y. Fei (2010), Internally consistent thermodynamic database for iron to the Earth's core
760 conditions, *Journal of Geophysical Research: Solid Earth*, *115*(B3).
761
762 Kunz, M., A. A. MacDowell, W. A. Caldwell, D. Cambie, R. S. Celestre, E. E. Domning, R. M. Duarte, A. E.
763 Gleason, J. M. Glossinger, and N. Kelez (2005), A beamline for high-pressure studies at the Advanced Light Source
764 with a superconducting bending magnet as the source, *Journal of synchrotron radiation*, *12*(5), 650-658.
765
766 Kunz, M., N. Tamura, K. Chen, A. A. MacDowell, R. S. Celestre, M. M. Church, S. Fakra, E. E. Domning, J. M.
767 Glossinger, and J. L. Kirschman (2009), A dedicated superbend X-ray microdiffraction beamline for materials, geo-,
768 and environmental sciences at the advanced light source, *Review of Scientific Instruments*, *80*(3), 035108.
769
770 Kunz, M., J. Yan, E. Cornell, E. E. Domning, C. E. Yen, A. Doran, C. M. Beavers, A. Treger, Q. Williams, and A.
771 A. MacDowell (2018), Implementation and application of the peak scaling method for temperature measurement in
772 the laser heated diamond anvil cell, *Review of Scientific Instruments*, *89*(8), 083903.
773
774 Laugier, J., and B. Bochu (2002), CELREF V3: Cell parameters refinement program from powder diffraction
775 diagram. Laboratoire des Matériaux et du Génie Physique, Institut National Polytechnique de Grenoble, France,
776 edited.
777
778 Liu, W., J. Kung, and B. Li (2005), Elasticity of San Carlos olivine to 8 GPa and 1073 K, *Geophysical Research*
779 *Letters*, *32*(16).
780
781 Liu, W., and B. Li (2006), Thermal equation of state of (Mg0. 9Fe0. 1) 2SiO4 olivine, *Physics of the Earth and*
782 *Planetary Interiors*, *157*(3-4), 188-195.
783

Manga, M., and R. Jeanloz (1996), Axial temperature gradients in dielectric samples in the laser-heated diamond cell, *Geophysical research letters*, *23*(14), 1845-1848.

Mao, H., J.-A. Xu, and P. Bell (1986), Calibration of the ruby pressure gauge to 800 kbar under quasi-hydrostatic conditions, *Journal of Geophysical Research: Solid Earth*, *91*(B5), 4673-4676.

Mao, W., G. Shen, V. B. Prakapenka, Y. Meng, A. J. Campbell, D. L. Heinz, J. Shu, R. J. Hemley, and H.-K. Mao (2004), Ferromagnesian postperovskite silicates in the D ″layer of the Earth, *Proceedings of the National Academy of Sciences of the United States of America*, *101*(45), 15867-15869.

Marquardt, H., and K. Marquardt (2012), Focused ion beam preparation and characterization of single-crystal samples for high-pressure experiments in the diamond-anvil cell, *American Mineralogist*, *97*(2-3), 299-304.

Meng, Y., D. J. Weidner, and Y. Fei (1993), Deviatoric stress in a quasi-hydrostatic diamond anvil cell: Effect on the volume-based pressure calibration, *Geophysical Research Letters*, *20*(12), 1147-1150.

Mezouar, M., R. Giampaoli, G. Garbarino, I. Kantor, A. Dewaele, G. Weck, S. Boccato, V. Svitlyk, A. Rosa, and R. Torchio (2017), Methodology for in situ synchrotron X-ray studies in the laser-heated diamond anvil cell, *High Pressure Research*, *37*(2), 170-180.

Morard, G., D. Andrault, D. Antonangeli, Y. Nakajima, A. Auzende, E. Boulard, S. Cervera, A. Clark, O. Lord, and J. Siebert (2017), Fe–FeO and Fe–Fe3C melting relations at Earth's core–mantle boundary conditions: Implications for a volatile-rich or oxygen-rich core, *Earth and Planetary Science Letters*, *473*, 94-103.

Murnaghan, F. D. (1951), *Finite deformation of an elastic solid*, John Wiley & Sons.

Ohtaka, O., H. Takebe, A. Yoshiasa, H. Fukui, and Y. Katayama (2002), Phase relations of AgI under high pressure and high temperature, *Solid state communications*, *123*(5), 213-216.

Panero, W., and R. Jeanloz (2001), Temperature gradients in the laser-heated diamond anvil cell, *Journal of Geophysical Research: Solid Earth*, *106*(B4), 6493-6498.

Prescher, C., and V. B. Prakapenka (2015), DIOPTAS: a program for reduction of two-dimensional X-ray diffraction data and data exploration, *High Pressure Research*, *35*(3), 223-230.

Rainey, E., and A. Kavner (2014), Peak scaling method to measure temperatures in the laser-heated diamond anvil cell and application to the thermal conductivity of MgO, *Journal of Geophysical Research: Solid Earth*, *119*(11), 8154-8170.

Shen, G., and H. K. Mao (2016), High-pressure studies with x-rays using diamond anvil cells, *Reports on Progress in Physics*, *80*(1), 016101.

Shen, G., H. k. Mao, R. J. Hemley, T. S. Duffy, and M. L. Rivers (1998), Melting and crystal structure of iron at high pressures and temperatures, *Geophysical Research Letters*, *25*(3), 373-376.

Shen, G., M. L. Rivers, Y. Wang, and S. R. Sutton (2001), Laser heated diamond cell system at the Advanced Photon Source for in situ X-ray measurements at high pressure and temperature, *Review of Scientific Instruments*, *72*(2), 1273-1282.

Shukla, G., M. Cococcioni, and R. M. Wentzcovitch (2016), Thermoelasticity of Fe3+-and Al-bearing bridgmanite: Effects of iron spin crossover, *Geophysical Research Letters*, *43*(11), 5661-5670.

Tamura, N., R. Celestre, A. MacDowell, H. Padmore, R. Spolenak, B. Valek, N. Meier Chang, A. Manceau, and J. Patel (2002), Submicron x-ray diffraction and its applications to problems in materials and environmental science, *Review of scientific instruments*, *73*(3), 1369-1372.

Tateno, S., T. Komabayashi, K. Hirose, N. Hirao, and Y. Ohishi (2019), Static compression of B2 KCl to 230 GPa and its PVT equation of state, *American Mineralogist*, *104*(5), 718-723.

Utsumi, W., N. Funamori, T. Yagi, E. Ito, T. Kikegawa, and O. Shimomura (1995), Thermal expansivity of MgSiO3 perovskite under high pressures up to 20 GPa, *Geophysical Research Letters*, *22*(9), 1005-1008.

Wang, Y., D. J. Weidner, R. C. Liebermann, and Y. Zhao (1994), PVT equation of state of (Mg, Fe) SiO3 perovskite: constraints on composition of the lower mantle, *Physics of the Earth and Planetary Interiors*, *83*(1), 13-40.

Williams, Q., E. Knittle, and R. Jeanloz (1991), The high-pressure melting curve of iron: A technical discussion, *Journal of Geophysical Research: Solid Earth*, *96*(B2), 2171-2184.

Figure 1.

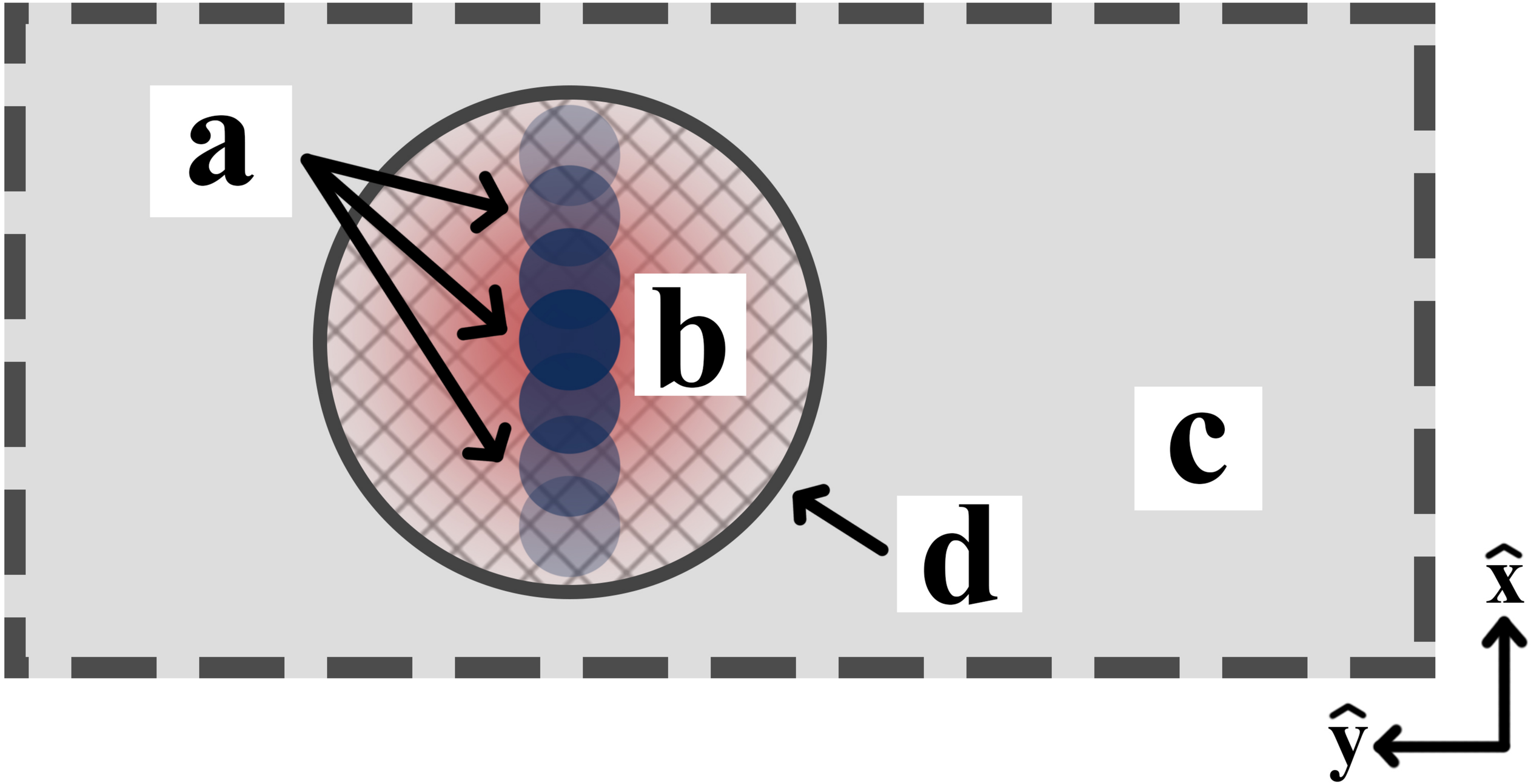
a
b
c
d
$\hat{x}$
$\hat{y}$

Figure 2.

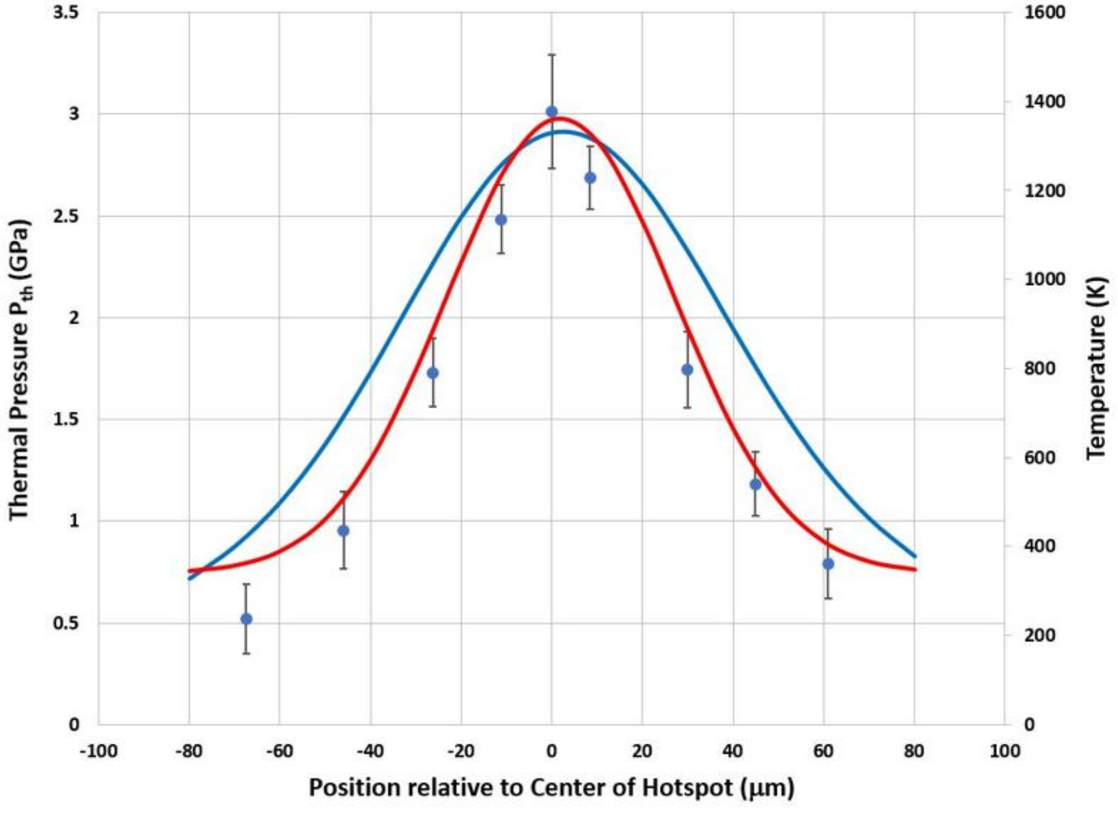
Thermal Pressure P_{th} (GPa)
Temperature (K)
Position relative to Center of Hotspot (μm)
3.5
3
2.5
2
1.5
1
0.5
0
1600
1400
1200
1000
800
600
400
200
0
-100
-80
-60
-40
-20
0
20
40
60
80
100

(a)

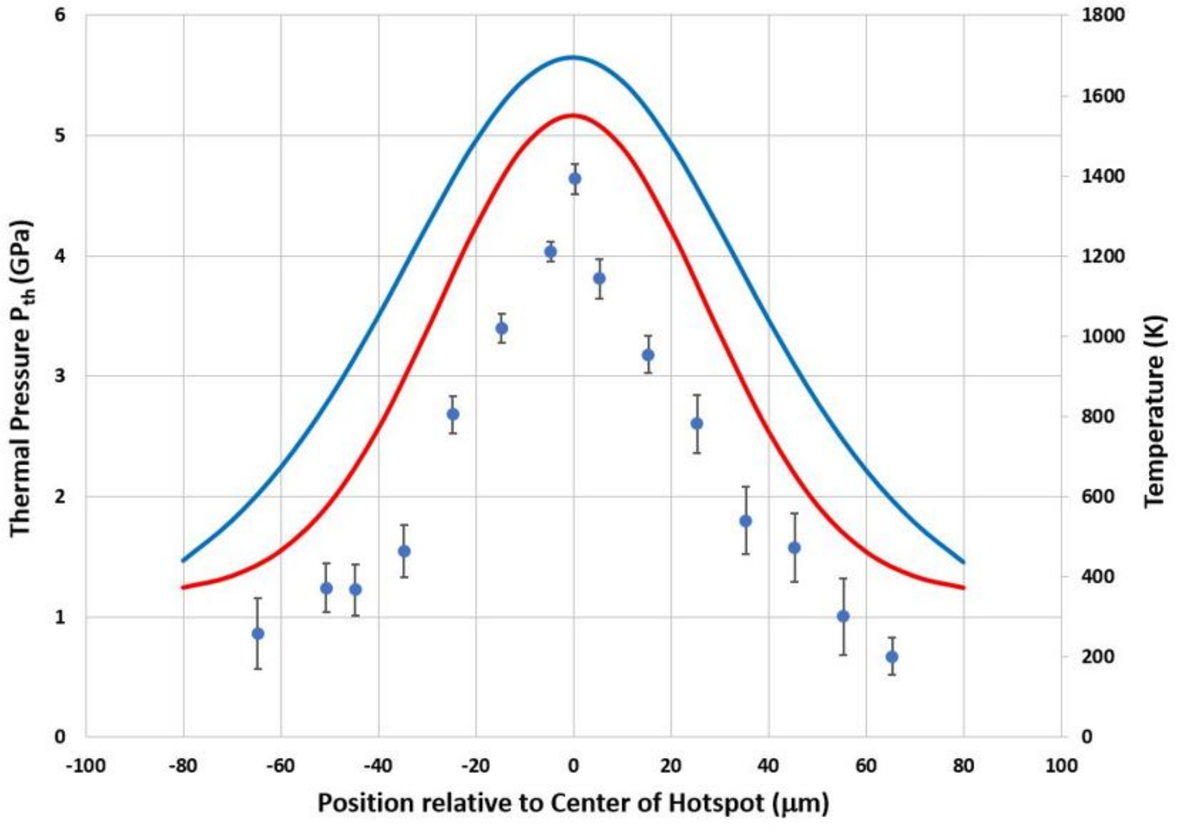
Thermal Pressure P_{th} (GPa)
Temperature (K)
Position relative to Center of Hotspot (μm)
6
5
4
3
2
1
0
1800
1600
1400
1200
1000
800
600
400
200
0
-100
-80
-60
-40
-20
0
20
40
60
80
100

(b)

Figure 3.

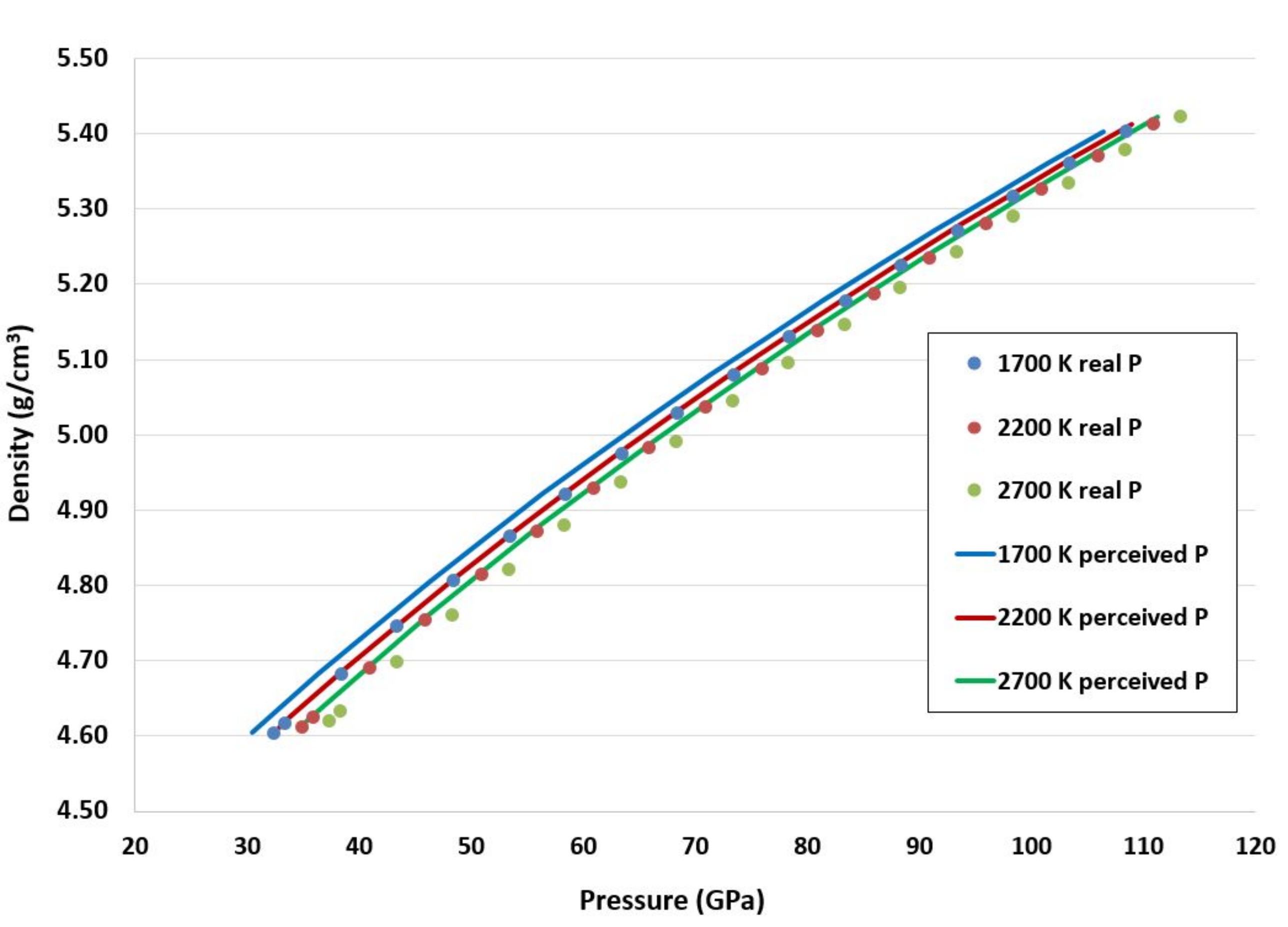
5.50
5.40
5.30
5.20
5.10
5.00
4.90
4.80
4.70
4.60
4.50
Density (g/cm³)
20
30
40
50
60
70
80
90
100
110
120
Pressure (GPa)
1700 K real P
2200 K real P
2700 K real P
1700 K perceived P
2200 K perceived P
2700 K perceived P